The role of starch in nano-magnetite formation: A spectrometric and structural investigation

Mbolantenaina Rakotomalala Robinson, Mustapha Abdelmoula, Martine Mallet, Romain Coustel

▶ **To cite this version:**

Mbolantenaina Rakotomalala Robinson, Mustapha Abdelmoula, Martine Mallet, Romain Coustel. The role of starch in nano-magnetite formation: A spectrometric and structural investigation. Materials Chemistry and Physics, inPress, 297, pp.127285. 10.1016/j.matchemphys.2022.127285 . hal-03937318

HAL Id: hal-03937318
https://hal.science/hal-03937318

Submitted on 13 Jan 2023

HAL is a multi-disciplinary open access archive for the deposit and dissemination of scientific research documents, whether they are published or not. The documents may come from teaching and research institutions in France or abroad, or from public or private research centers.

L'archive ouverte pluridisciplinaire **HAL**, est destinée au dépôt et à la diffusion de documents scientifiques de niveau recherche, publiés ou non, émanant des établissements d'enseignement et de recherche français ou étrangers, des laboratoires publics ou privés.

Distributed under a Creative Commons Attribution - NonCommercial - NoDerivatives 4.0 International License

The role of starch in nano-magnetite formation: a spectrometric and structural investigation

Mbolantenaina Rakotomalala Robinson, Mustapha Abdelmoula, Martine Mallet, Romain Coustel*
CNRS, LCPME, Université de Lorraine, 54600 Nancy, France

Keywords:
Magnetic nanoparticles
Superparamagnetic materials
Magnetite
Polysaccharide
Raman
Mössbauer spectroscopy

Abstract

In the framework of pollutant sequestration by magnetic nano materials, this work focuses on the synthesis and the physico-chemical properties of starch functionalized nano magnetites. Nanoparticles were prepared by the Fe^{2+}/Fe^{3+} coprecipitation method with increasing amount of starch in the synthesis medium (starch to iron mass ratio (R) in the range 0-10). Obtained materials were characterized by Transmission Electron Microscopy (TEM), Powder X-Ray Diffraction (PXRD), Raman, Fourier Transform Infrared (FTIR) and ^{57}Fe Mössbauer spectroscopies, as well as by vibrating sample magnetometry. The presence of starch into the synthesis medium lowers magnetite crystallinity and increases the dispersion of the oxide particles. Both effects lead to fast relaxing superparamagnetic particles at RT for high R. The role of starch on nano-magnetite growth and stabilization is evidenced.

Introduction:

Magnetic nanoparticles (NP) have been attracting strong interest for the past decades due to their established as well as novel applications in the fields of data storage (Dai and Nelson, 2010), medicine (contrast agents for biomedical imaging and drug or gene delivery) (Hah et al., 2021; Hong et al., 2007; Miyamoto et al., 2012; Uthaman et al., 2015; Zhang et al., 2013), purification and extraction of bio-macromolecules (Eivazzadeh-Keihan et al., 2021), catalysis (Iyengar et al., 2016; Zhang et al., 2019), etc. Due to their high specific area, that provide high adsorption properties, NP are also considered for environmental processes (Bée et al., 2017; Ren et al., 2017; Yoon et al., 2017). In this respect, the benefit of additional magnetic properties is that the adsorbent could be separated from contaminated water via a weak magnetic separator. To prevent particles agglomeration and, then, to preserve their specific area, organic functionalization appears as an efficient strategy. Thanks to their low-toxicity, abundance and cost-effectiveness, both polysaccharides and iron oxides are relevant building blocks for the design of ecofriendly materials for environmental (Rakotomalala Robinson et al., 2020) but also medical (Miyamoto et al., 2012) applications.

From a fundamental point of view, the development of polysaccharide functionalized iron oxide NP raises, at least, two questions. Firstly, the nature of the molecular bonds between polysaccharide and iron oxide remains puzzling. Actually, the strong affinity between polysaccharide and iron oxide is well established and has long been used on an industrial scale, e.g. starch has been used as universal depressant in reverse flotation of iron oxide in the field of mineral processing (Pattanaik and Venugopal, 2018). Nevertheless, adsorption mechanisms are misunderstood: complexation with metal site (Laskowski et al., 2007; Weissenborn et al., 1995), hydrogen bonding (Filippov et al., 2013; Ma, 2008) or hydrophobic interactions (Laskowski et al., 2007) were proposed. A recent DFT calculation study(Li et al., 2019) concludes that starch adsorbs on hematite through direct chemical bonds and hydrogen bonds involving water molecules.

For a greater economic and environmental efficiency, it appeared relevant to synthesize NP and to functionalize them in a single synthesis step where iron oxide is precipitated into a polysaccharide solution. This raises the second question of how polysaccharides, and more widely polymers, affect NP formation. Two steps, nucleation and growth(Jolivet et al., 2000; LaMer and Dinegar, 1950; Mutaftschiev, 2001), lead to crystal formation but the impact of polysaccharides is scarcely described in literature. Polymer chains can behave as nucleation point for oxide: carboxylate and amine functions are able to form complexes with aqueous $Fe^{2+/3+}$ ions or to bind NP oxide. So NP formation can take place into alginate (Hernández et al., 2009) or chitosan (Wang et al., 2008) gels as well as into an interpenetrating (carboxymethyl cellulose/chitosan) polymer network (Kaihara et al., 2011). It has been demonstrated that iron complexation could be tapped to favor formation of NP into poly(acrylic acid) brushes (Zhu et al., 2012) or along a DNA strand.(Sarkar and Mandal, 2012) Several studies reported the synthesis of iron oxyhydroxide NP in presence of carrageenan. In these conditions, self-assembled polysaccharide behaves as nano-reactor providing localized area for iron hydrolysis and particle growth (Jones et al., 2000; Rashid et al., 2014). Carrageenan was claimed to stabilize iron oxide NP and to prevent their agglomeration. In spite of these examples, some authors pointed out that in-depth understanding of the mechanisms at play when oxide NP were prepared in presence of polymer remained unclear and challenging (Noqta et al., 2019).

This work aims to get further insight on how polysaccharides affects iron oxide NP formation. As magnetite (Fe_3O_4) presents one of the highest saturation magnetizations among the iron oxides (92 emu g^{-1} at room temperature (Han et al., 1994)), we will focus on nano magnetite prepared by coprecipitation of Fe^{2+} and Fe^{3+} in alkaline condition with an increasing amount of starch. Actually, it should be note that the nucleation and growth of NP can be hardly tracked during the synthesis. In this paper, we restrict ourselves to characterize the obtained materials to infer the role of starch. NP were fully analysed by Transmission Electron Microscopy (TEM), Powder X-Ray Diffraction (PXRD), Raman, Fourier Transform Infrared (FTIR) and ^{57}Fe Mössbauer spectroscopies, as well as by vibrating sample

magnetometry. Because of its unique ability to finely probe Fe-Fe interactions, Mössbauer spectroscopy allows to spot starch induced modification of the iron oxide NP. In particular, superparamagnetic behaviors of the NP were correlated to starch content. It comes that starch is able to disperse and stabilize iron oxide NP with reduced crystallinity.

Methods

Materials

All chemicals used in this work (obtained from multiple suppliers) were of analytical grade and used without further purification: ferrous sulphate heptahydrate ($FeSO_4.7H_2O$, Fisher Chemical), ferric chloride hexahydrate ($FeCl_3.6H_2O$, Sigma-Aldrich) potassium hydroxide (KOH, Riedel-de Haën), potassium nitrate (KNO_3, Merck), ethanol 96% (VWR) and soluble starch (Sigma-Aldrich). Ultrapure water (18.2 MΩ cm^{-1}) was used for the all experiments. Water was previously bubbled at least 1 h with N_2 before use to prevent uncontrolled iron oxidation.

Synthesis of magnetic nano-particles

Magnetite nano-particles were prepared by coprecipitation of Fe^{2+} and Fe^{3+} with a base. Our protocol was established on the basis of the work of several authors (Chang et al., 2011; Culita et al., 2008; Gnanaprakash et al., 2007b, 2007a; Liang et al., 2012). Typically, 70 mL of a solution containing Fe^{2+} and Fe^{3+} ions in a 2:1 molar ratio was prepared by dissolving 1130 mg of $FeCl_3.6H_2O$ and 581 mg of $FeSO_4.7H_2O$ in 0.1 M HCl solution. The dissolution was performed under nitrogen bubbling. The resulting mixture was heated to 80°C. Once the temperature was reached, 10 mL of a concentrated ammonia solution was added rapidly at one time to the reaction medium and the resulting suspension was heated for 10 minutes at the temperature of 80°C. Then, the suspension was cooled and aged overnight. Before washing, a neutralization step was necessary. For that purpose, concentrated hydrochloric acid (HCl) was added to the suspension to lower the pH to 7. The black precipitate was recovered by centrifugation, washed 5 times with ultrapure water and then 1 time with ethanol (96%) to remove the unreacted reagents. The resulting product was dried under vacuum.

For the synthesis of starch functionalized NP, the synthesis method was slightly modified. Starch was gelatinized in the iron solution before the addition of the base. The starch to Fe mass ratio (R) ranged from 0 to 10 (R = 0 corresponds to starch free NP, R = 10 corresponds to 3500 mg of starch). The following steps remained the same as the ones for the starch free sample. The samples obtained by coprecipitation (CP) were labelled CP-RX where the number X corresponds to the starch to iron mass ratio, which constitutes the only varying parameter of this set of samples.

An additional sample labelled CP-R10After was prepared adding gelatinized starch (R = 10) after Fe^{2+} and Fe^{3+} ions coprecitiation: 15 min after base introduction, starch was added to synthesis medium (the protocol for particle aging and particle recovery remained unchanged).

Materials characterization

Transmission electron microscopy (TEM) and scanning electron microscopy (SEM) were used to ascertain the morphology of the as-prepared NP. The TEM micrographs were obtained on a JEOL 2100F and Philips CM200 microscopes both operating at an accelerating voltage of 200 kV. The samples were dispersed in ethanol (96%) under ultrasound. One drop of suspension was deposited on a metal grid covered with a carbon film. The SEM micrographs were obtained on a JEOL JSM-IT500HR operating at an accelerating voltage of 5.0 kV.

Powder X-Ray Diffraction (PXRD) patterns were recorded with an X'Pert Pro diffractometer (PANalytical) equipped with a copper anode X-ray tube and a Ge(111) monochromator to exclude the $K\alpha_2$ line. Then, diffractograms were recorded with the only Cu $K\alpha_1$ line ($\lambda(K\alpha_1)$ = 1.5406 Å).
Raman spectra were recorded on an inVia Qontor spectrometer (Renishaw) equipped with a Leica confocal microscope. The wavelength of the laser beam used was always 532 nm and the objective had a magnification ×50. The scattered light was collected by the same objective and then passed through a diffraction grating (2400 lines/mm). The scattered light was collected by a Peltier cooled CCD detector. A power of 0.05 mW at the sample level was used.
The infrared spectra were acquired with a Vertex 70v spectrometer (Bruker) in transmission mode. The absorption bands of CO_2 and water vapor were limited by the use of vacuum. The sample to be analyzed (0.5 mg) was ground with KBr (150 mg) in an agate mortar and compressed with a hydraulic press. For each sample, 100 spectra with a resolution of 4 cm^{-1} had been collected in the wavenumber range from 100 to 6000 cm^{-1}.
^{57}Fe Mössbauer spectra were collected using two conventional spectrometers in transmission geometry coupled with a cold head cryostat from Advances Research Systems (USA) or JANIS Research (USA), equipped with vibration isolation stand, developed in LCPME laboratory. The 50 mCi ^{57}Co in Rh matrix radioactive source was mounted in a constant acceleration velocity transducer. Measurements were taken at the wide range of velocity ±11 mm s^{-1}. The hyperfine interaction parameters were determined by fitting the experimental spectra by a least-squares method using the Recoil software (K. Lagarec and Rancourt, 1998). The center shifts were reported with respect to that of 25 µm-thick α-Fe foil at room temperature. A commercial MicroSense vibrating sample magnetometer was used to measure magnetic moment versus magnetic field amplitude at room temperature. The powder was place in quartz cup fixed onto a quartz sample rod.

Results

TEM

TEM micrographs evidenced that the coprecipation method provides finely dispersed iron oxide (see Fig. 2). In the absence of starch (CP-R0), round-shaped particles with diameter equal to 13 ± 3 nm were obtained (see Fig. S1). The orientation of lattice fringes probed by high resolution TEM allows to distinguish individual crystallites within aggregates. With starch to iron mass ratio equal to 10 in the synthesis medium, CP-R10 appears as flake of starch where particles seem incorporated (observed where the polymer matrix is thin enough to be transparent). Particles also present round shape when prepared with high amount of starch but show lower diameter (< 10 nm) than CP-R0.
The corresponding selected area electron diffraction (SAED) patterns are displayed in Fig. 2. The CP-R0 material gives rings that can be indexed according to the inverse spinel iron oxide phase (JCPDS 19-0629). The spotty character of the rings is due to the limited number of probed crystallites. The SAED pattern of CP-R10 material can be indexed in the same way. Nevertheless, in the latter case both the extinction of several rings and the strengthening of the diffuse character of the rings should be attributed to poorer crystallinity of the oxide phase synthesized in presence of starch.

PXRD

To complete the microstructure analysis, the obtained products were further characterized by PXRD (see Fig. 3). In line with SAED results, CP-R0 obtained by the coprecipitation pathway shows PXRD pattern that can be indexed according to the magnetite structure (JCPDS 19-0629). The positions of the diffraction peaks remain unchanged when starch is introduced into the synthesis medium showing that the inverse spinel iron oxide structure is essentially preserved for CP-R0.31 to R10. For high value of R (R5, R10), starch gives a wide hump in the 10-25° region. The diffraction peaks of the iron oxide phase broaden with increasing value of R, evidencing the size reduction of the crystallites. The average crystallite dimensions *<d>* were evaluated applying the Scherrer's formula (Scherrer, n.d.; Suryanarayana and Norton, 2014) on the two most intense peaks (311) and (440) using X'Pert Highscore Plus v2.2b software. It appears that *<d>* tends to diminish with increasing starch amount: *<d>* equals 13.7 ± 0.4, 13.7 ± 0.6, 12.6 ± 0.4, 8.5 ± 0.4 and 8.8 ± 0.4 nm for R0, R0.31, R2, R5 and R10, respectively. One should note that magnetite and maghemite are both inverse spinel iron oxides with rather similar diffractogram (Cornell and Schwertmann, 2003) (see reference diffractograms for magnetite (JCPDS 19-0629) and maghemite (JCPDS 39-1346) in Fig. 4). Then, these phases are hardly distinguishable from PXRD measurements in particular when poorly crystallized or nanomaterials solids are considered. In here, definitive phase identification needs additional characterization by Raman and Mössbauer spectroscopies.

Raman spectroscopy

The Raman spectrum of the CP-R0 sample (Fig 4) presents bands at 670, 540 and 310 cm^{-1} attributed, respectively, to the A_{1g}, T_{2g} and E_g modes of magnetite (de Faria et al., 1997; Shebanova and Lazor, 2003). It should be noted that maghemite is expected to give Raman bands at 350, 500, 660 and 715 cm^{-1} as well as a broad band at ~1400 cm^{-1} (Boucherit et al., 1989; de Faria et al., 1997; Hanesch, 2009; Jacintho et al., 2007; Ohtsuka et al., 1986). The absence of these bands excludes maghemite phase in R0 samples at least in a minute amounts that could be detected by Raman spectroscopy.

The bands originating from starch (see reference spectrum in Fig 4) arise for increasing value of R and they overlap with the weak T_{2g} and E_g bands (similarly FTIR spectra present starch bands for increasing value of R confirming magnetite functionalization, see Fig S2). Concurrently, when R value is above 2, a shoulder at 710 cm^{-1} widens the main A_{1g} magnetite band. As discussed bellow, this broadening may be attributed to starch induced defect into magnetite structure.

Mössbauer spectrometry

Mössbauer ^{57}Fe spectrometry measurements were performed to get a further insight into the impact of starch on both structural and magnetic properties of the CP materials. The Mössbauer spectra recorded from room temperature (RT) to 13 K on CP-R0, CP-R5 and CP-R10 are given in Fig. 5 while the corresponding hyperfine parameters are given in Table 1.

In sake of clarity, let us compare these spectra to the ones of reference magnetite (labelled OP-R0) prepared according to the oxidation precipitation method (Schwertmann and Cornell, 2000) (see Fig. S4 and table 1). RT spectrum shows two sextets with hyperfine parameters equal to CS = 0.28 mm s^{-1} / H_{hf} = 49.0 T and CS = 0.66 mm s^{-1} / H_{hf} = 45.8 T. These sextets are assigned to Fe^{3+} in tetrahedral site (S_A) and $Fe^{2.5+}$ in octahedral site (S_B), respectively according to results obtained on bulk magnetite or particles whose size is >30 nm (Byrne et al., 2013; Daou et al., 2006; Vandenberghe et al., 2000). According to the recommendation of Zegeye et al. (Zegeye et al., 2011), the deviation (δ) from the ideal stoichiometry ($Fe_{3-\delta}O_4$) can be evaluated from the relative area of S_A and S_B. It comes δ = 0.01 indicating that OP-R0 is very close to pristine magnetite and confirming PXRD and Raman spectroscopy results.

Below Verwey transition that occurs at 120 K (Daniels and Rosencwaig, 1969; Verwey, 1939), the crystallite structure of magnetite undergoes a symmetry changes from cubic to monoclinic, while the electron hopping between Fe^{3+} and Fe^{2+} ions located in octahedral sites ceases freezing this process. As a consequence, the Mössbauer spectrum of magnetite at low temperature is relatively complex (Sawatzky et al., 1969; Srivastava et al., 1981). Nevertheless, it is commonly accepted that low temperature spectra can be fitted with five sextets assigned to Fe^{3+} and Fe^{2+} in tetrahedral and octahedral sites. Such an approach was successfully applied to the spectrum recorded on OP-R0 at 4 K (Fig. S4). A particular feature is a sextet that presents a low hyperfine field (34.1 T) with respect to the remaining four components and comparatively higher center shift (CS) and quadrupole shift (ε). This sextet represents 10 % of the relative area and it is attributed to Fe^{2+} in octahedral site (Daou et al., 2007; Srivastava et al., 1981).

At RT, CP-R0 is composed of six broad lines suggesting hyperfine fields distributions (HFD). Satisfactory fit was obtained with two HFD sites (*CS* = 0.27 mm s^{-1} / $\langle H_{hf} \rangle$ = 44.0 T and *CS* = 0.54 mm s^{-1} / $\langle H_{hf} \rangle$ = 35.1 T, see Fig. 5) assigned to tetrahedral and octahedral ions, respectively. The deviation from ideal stoichiometry derived from the relative area of S_A and S_B (Zegeye et al., 2011) is low (δ = 0.03). This result supports Raman analysis that ruled out maghemite contribution. It is particularly noteworthy that CP-R0 shows Fe^{2+} content close to the one of stoichiometric magnetite. Actually, significant oxidation is often reported small nano magnetite (particle size ~10 nm) with $Fe^{3+}/Fe^{2.5+}$ Mössbauer ratio component above 2.5 (Amir et al., 2015; Kotsikau et al., 2018) or even no $Fe^{2.5+}$ component (Güner et al., 2016), which suggests the formation of maghemite.

The Mössbauer spectrum of CP-R0 recorded at 20 K corresponds to low temperature magnetite footprint (Fig. 5) confirming the identification of the dispersed phase. It is noteworthy that the relative weight of S_5 (high *CS* = 0.90 mm s^{-1}, high ε = 1.72 mm s^{-1} and low $\langle H_{hf} \rangle$ = 34.9 T) is only 3 % compared to 10 % for OP-R0. Although S_5 is attributed to a fraction of Fe^{2+} ions, its weakness does not match with low δ (poorly oxidized magnetite).

When prepared with starch, the CP samples show substantially different Mössbauer profiles. CP-R5 spectrum at RT presents a broadening of measured spectral lines (superposition of broad sextets and central lines) (Fig. 5). For CP-R10 that corresponds to higher amount of starch, no more magnetic component was observed at RT but this component rises and gradually grows with decreasing temperature (Fig. 5), which is typical of superparamagnetic behavior. Following the procedure proposed by Tronc et al. for superparamagnetic nano-maghemite, CP-R5 and CP-R10 spectra were fairly reproduced with three components (Tronc et al., 1995). A quadrupole doublet, a magnetically split component, and a broad single line are attributed to particles in the superparamagnetic state, in the blocked state and with intermediate relaxation times, respectively. Below the Verwey transition, the remaining magnetic components correspond to magnetite.

Magnetization measurements

The magnetic properties of the hybrid materials were estimated from the specific magnetization curves as a function of magnetic field strength recorded at room temperature (Fig 6). All the samples show curves wich can be fitted with Langevin functions characteristic of superparamagnetic behaviour of nanoparticules. The saturation magnetizations (*Ms*) of the materials CP-R0, CP-R5 and CP-R10 are 63.5, 19.3 and 8.4 emu g^{-1} (as derived from Langevin function fits, see Fig 6). All CP materials present the typical superparamagnetic behavior, the absence of hysteresis loop is assigned to the small size of the NP having a single magnetic domain.

The value obtained for the starch free material (CP-R0) is lower than the theoretical value of the bulk magnetite (92 emu g^{-1} (Han et al., 1994)). Previous reports on Fe_3O_4 NP (Amir et al., 2016; Byrne et al., 2013; Daou et al., 2008, 2006; Kotsikau et al., 2018; Meite et al., 2022b, 2022a; Zegeye et al., 2021) indicated that *Ms* decreases with particle size (see inset of Fig 6). Our results on CP-R0, as well as on OP-R0 (*Ms* = 89.1 emu g^{-1} for 67 nm particles), are fully consistent with the reported trend. *Ms* lowering is attributed to the surface contribution: spin canting, surface disorder, stoichiometry deviation, cation distribution and adsorbed water.(Daou et al., 2006) Hybrid materials (CP-R5 and CP-R10) show an even lower *Ms* than uncoated ferrite NP because of the reduced content of magnetic oxide (Amir et al., 2017; Baykal et al., 2015; Covaliu et al., 2011).

Discussion

Coprecipitation vs oxidation precipitation

In a recent study (Rakotomalala Robinson et al., 2019), we reported characterizations of starch functionalized spinel iron oxide NP obtained by the oxidation-precipitation method (Schwertmann and Cornell, 2000). In brief, this method consists of the partial oxidation of an Fe^{2+} solution in alkaline medium by nitrate. The OP method was modified by introducing gelatinized starch in the Fe^{2+} solution before the addition of the base. Then, starch functionalized NP were prepared with a starch to iron mass ratio varying in the range of 0 to 10 (labelled from OP-R0 to OP-R10).

TEM measurements revealed that in the absence of starch OP-R0, the oxidation-precipitation path leads to cubic shape particles with much higher average size (80 ± 30 nm) than CP-R0 (13.7 ± 0.4 nm). As reported in this paper for CP method, increasing the amount of starch tends to reduce the size of the NP when prepared according to the OP method. But contrary to CP samples, OP-R10 also presents intriguing objects with rough surface (corrugation length of <10 nm) and shows lattice fringes, and then crystalline order, of several tens of nanometer.

The PXRD patterns of the OP samples evidences the presence of spinel phase, whose crystallinity decreases when the amount of starch is increased: $\langle d \rangle$ drops from 67 ± 5 nm for OP-R0 to 44 ± 4 nm for OP-R0.31 and reaches 12 ± 4 nm for R10. Then, PXRD (as well as TEM and SAED) suggests that the functionalized CP particles are smaller than the ones obtained by the OP method and they also present narrower crystallite size distribution. Moreover, non-indexed diffraction peaks were reported for OP-R5 and OP-R10 while no extra crystallized phase can be suspected from PXRD records on CP products.

Although CP-R0 ($\langle d \rangle$ = 13.7 ± 0.4 nm) presents poorer crystallinity than OP-R0 ($\langle d \rangle$ = 67 ± 5 nm), their Raman spectra present no difference (see Fig. 4 and (Rakotomalala Robinson et al., 2019)). This observation confirms that without starch the two synthesis routes lead to magnetite formation and highlights that Raman fingerprint of magnetite weakly depends on crystallite size (at least for $\langle d \rangle$ > 14 nm). Therefore, the asymmetry of the A_{1g} band that was observed on OP-R2 ($\langle d \rangle$ = 30 ± 10 nm) cannot be attributed to size effect, but instead should be ascribed to defects due to partial oxidation and/or starch/oxide interactions (Kumar, 2012). A similar cause may explain the shoulder (710 cm^{-1}) of the A_{1g} band for CP-R5 and CP-R10.

While both CP and OP samples show similar PXRD patterns and Raman profiles, Mössbauer spectrometry clearly discloses additional consequences of the reduced crystallite size. Due to its selectivity on the element iron, the Mössbauer effect is very sensitive to hyperfine interactions and allows access to both magnetic properties and their relationship to the size-dependent effect of very small particles. This point will be discussed in the next section.

^{57}Fe Mössbauer fingerprint of starch functionalized nano magnetites

In this study, magnetic properties of the nano materials were probed by Mössbauer spectrometry. The magnetic moment of nano-sized particle is subject to thermally driven fluctuation. The magnetic anisotropy of a single-domain particle is proportional to its volume (V) and its anisotropy energy is given by:

$$E = K.V.\sin^2(\theta) \quad (1)$$

where K is the magnetic anisotropy constant and θ is the angle between the (sublattice) magnetization vector and the easy axis. Therefore, if the volume is small, the energy barrier between two energy minima drops down to the range of thermal energy. In the high temperature (T) regime, the reversal of the magnetic moment among the easy direction of magnetization arises, which corresponds to superparamagnetic relaxation. At low temperature, the direction of the magnetic moment is retained. For isolated (non-interacting) particle, the Néel relaxation time τ_N of the process is given by(Néel, 1949):

$$\tau_N = \tau_0 . \exp\left(\frac{K.V}{k_B.T}\right) \quad (2)$$

where τ_0 is a constant in the range of 10^{-9}-10^{-12} s depending on the material, *K* the magnetic anisotropy constant, and k_B the Boltzmann's constant.

If τ_N is larger than the Mössbauer measurement time (3 10^{-8} s), the probed nucleus behaves as in steady magnetic surrounding giving rise to a magnetically split sextet. For low τ_N, fluctuation throughout the measurement time tends to reduce average magnetization and then, sextet collapses into one or two paramagnetic lines (Fock et al., 2018). Nevertheless, the Néel's model is not sufficient to explain the asymmetric broadening of the Mössbauer lines observed for CP-R0 at RT. Actually, superparamagnetic behavior depends also on particle size distribution, particle morphology, surface effects as well as inter-particle interaction (dipole-dipole interaction and exchange interaction) (Fock et al., 2018; Tronc et al., 1995). Theoretical description of inter-particle interaction is a complex issue whose theoretical description is controversial (Dormann et al., 1999; Mørup et al., 2010). According to Mørup et al. inter-particle interaction may result in a blocking or ordering of the magnetic moments of the particles. Then, the magnetic energy of a particle can be calculated using the superferromagnetism model in the framework of the mean-field model for interacting nanoparticles (Fock et al., 2018; Mørup et al., 1983):

$$E \approx K.V.\sin^2(\theta) - J_{eff}.{M_0}^2(T).b(T).\cos(\theta) \quad (3)$$

where J_{eff} is an effective interaction constant describing the magnetic interaction between a particle with its neighbors, M_0 is the magnetization of a particle and *b(T)* is an order parameter of the magnetic moments of the particles. *b(T)* is a parameter in the range 0-1 that decreases with increasing temperature as the direction of the magnetization fluctuate. When magnetic fluctuations are fast compared to the Mössbauer measurement time, the magnetic hyperfine splitting is proportional to *b(T)*. Distribution of anisotropy energies and interaction energies will end to in a distribution of b, which results in sextets with asymmetrically broadened lines for CP-R0 at RT. At lower temperature, the increase of b leads to narrower hyperfine field distribution and, then, to narrower sextet lines as observed at 145 K (Fig 5).

According to equation 3, the particle size reduction and the dispersion of the particles into a matrix cause the weakening of both anisotropy energy and interaction energy, which in turn favor the relaxation process. The results presented in this paper are consistent with this trend. At RT, CP materials present Mössbauer spectra that evolve from magnetic profile to central single line for increasing R. Actually, starch tends to reduce crystallite size and leads to an overall dispersion of the magnetic particles.

To get a further insight into the role of starch into the growth of the spinel phase, particles were prepared by the CP method: gelatinized starch was added 15 min after base introduction (ammonia) into the reactive medium (the protocol for particle aging and particle recovery was unchanged). The PXRD pattern of the obtained material (labelled CP-R10After) corresponds to iron oxide spinel with $\langle d \rangle_{CP\text{-}R10After}$ = 11.8 ± 1 nm. Raman lines at 667, 540 and 310 cm^{-1} confirms magnetite formation while FTIR probes starch fraction (see Fig 7 and S3). Interestingly, the Mössbauer spectra of CP-R10After recorded at RT and 4 K show similar profile to that of CP-R0 (see Fig 7) with close hyperfine parameters (see Table 1). This result highlights the importance of starch during the spinel growth. Actually, starch addition after coprecipitation leads to the formation of iron oxide with structural properties close to the ones of CP-R0. This is probably due to the formation of crystallite aggregates whose size is sufficient to show similar magnetic properties as CP-R0. This assumption is supported by SEM picture that shows micrometer-sized aggregates of crystallites deposited on starch (see Fig 7). Then, starch addition after coprecipitation does not result into disperse oxide crystallites. One can infer that, when present during precipitation, starch prevents crystallites aggregation. This result is in accordance with adsorption ability of CP materials. As reported previously, the arsenate adsorption capacity of CP-R10 is more than 4 times stronger than for CP-R0 (Rakotomalala Robinson et al., 2020). Such difference should be mainly attributed to limited agglomeration that preserves the specific surface area (the particle size reduction could only explain an increase of the adsorption capacity by a factor close to 1.6).

For CP pathway, rapid addition of ammonia favors oxide nucleation. Nevertheless, the presence of starch during precipitation tends to reduce the crystallite size, which can be attributed to an

exacerbated nucleation. Actually, starch may alter particles formation in several ways: polymer chains may (i) limit the diffusion of molecular species toward growing crystallites, (ii) stabilize the surface of small particles, (iii) act as nucleation points. Both (ii) and (iii) would result in iron oxide intimately mixed with organic phase. It is worth noticing that the inclusion of polymer chains inside nano-magnetite particles was considered for synthesis in the presence of carboxymethylcellulose (Maccarini et al., 2014). In here, starch inclusion may contribute to the decay of spinel crystallinity and in turn to the weakening of Fe-Fe interactions and the strengthening of the relaxation process for high R.

Then the magnetic behavior of the nano-materials obtained by the CP methods can be roughly rationalized considering that increasing value of R induces the reduction of the spinel iron oxide crystallites size (possibly by starch inclusion into the oxide structure), as well as the overall increasing of the inter particle distances. These factors would favor relaxation process.

All these results lead to infer that during synthesis starch chains contribute to isolate NP from each other. Then starch would behave as nano-reactor providing localized area for iron hydrolysis and particle growth, which is role of carrageenan when iron oxyhydroxide NP are prepared (Jones et al., 2000; Rashid et al., 2014).

Comparing both CP and OP materials bring some light on the role of starch upon the nanostructuration of the spinel iron oxide. In the absence of starch, the OP pathway gives smooth and sharp edge magnetite particles (67 ± 5 nm) showing magnetic properties close to bulk material. The increase of R value up to 10 strongly affects both microstructural and magnetic properties. Crystallite size declines with starch amount. For OP-R10, crystallite diameter drops down to 12 ± 4 nm (Rakotomalala Robinson et al., 2019) and lies in between the ones of CP-R0 and CP-R10 in spite of quite dissimilar magnetic properties as probed by Mössbauer spectrometry. At RT, the spectrum of OP-R10 is the sum of a magnetic component and a doublet whose contribution vanishes at lower temperature. Such features have to be attributed to the peculiar structures obtained through the OP pathway. Actually, the HRTEM micrographs of OP-R10 evidence corrugated crystallites with serrated edge, which suggests that starch induces defects preventing even growth of the oxide crystals. It appears that starch decisively steers the growth and the structural properties of the nano iron oxide spinel phase.

Conclusions

In this study, we paid attention to how the properties of nano-magnetite prepared by coprecipatation pathway are altered when gelatinized starch is introduced into the synthesis medium (iron to starch mass ratio in the range 0-10). PXRD shows the spinel structure of the oxide is preserved when starch is used but with lower crystallinity (the crystallite size is reduced from 13.7 ± 0.4 nm for CP-R0 to 8.8 ± 0.4 for CP-R10). Raman and Mössbauer spectroscopies show that, in absence of starch, coprecipitation leads to the formation of nearly stoichiometric magnetite, while increasing R leads to material containing defective magnetite. All CP materials present superparamagnetic behavior but Mössbauer spectrometry allows to evidence distinct magnetic properties. Starch lowers magnetite crystallinity and increases crystallites dispersion, both effects contribute to exacerbate relaxation process (Fock et al., 2018), which leads to fast relaxing superparamagnetic particles embedded in starch matrix.
When gelatinized starch is added in the synthesis medium after coprecipitation, the obtained oxide shows similar properties as starch free material. This result highlights the role of starch to steer the growth of nano-magnetite. One can infer that in the synthesis medium, starch chains could provide nucleation points and localized volume for iron hydrolysis and particle growth. Moreover, the presence of starch into the synthesis medium during Fe^{2+} and Fe^{3+} precipitation prevents particles agglomeration, which is of prime importance to elaborate competitive magnetic adsorbent.
Finally, comparison with materials obtained in the presence of starch through the oxidation precipitation pathway illustrates the diversity of the structural and magnetic properties that can be reached. It appears that a wide range of easy-to-prepare and ecofriendly nanostructured materials is at hands by using polysaccharide to control oxide synthesis.

Acknowledgements

The authors would like to thank Sylvie Migot (IJL-Nancy), Jaafar Ghanbaja (IJL-Nancy) and Liva Dzene (IS2M, Mulhouse) for TEM imaging. We thank the PMD2X X-ray diffraction facility and Pierrick Durand (CRM2-Nancy), for X-ray diffraction measurements, data processing and analysis, and providing of reports for publication: http://crm2.univ-lorraine.fr/lab/fr/services/pmd2x. FTIR, Raman and Mössbauer spectrometric measurements were performed at the spectroscopy and microscopy service facility of SMI LCPME (Université de Lorraine-CNRS– http://www.lcpme.cnrs-nancy.fr). The authors would like to thank Stephane Suire and CC MagCryo (IJL-Nancy) for help with magnetometry measurements.

Bibliography

Amir, Md., Baykal, A., Güner, S., Güngüneş, H., Sözeri, H., 2016. Magneto-optical investigation and hyperfine interactions of copper substituted Fe3O4 nanoparticles. Ceram. Int. 42, 5650–5658. https://doi.org/10.1016/j.ceramint.2015.12.089

Amir, Md., Güner, S., Yıldız, A., Baykal, A., 2017. Magneto-optical and catalytic properties of Fe3O4@HA@Ag magnetic nanocomposite. J. Magn. Magn. Mater. 421, 462–471. https://doi.org/10.1016/j.jmmm.2016.08.037

Amir, Md., Ünal, B., Geleri, M., Güngüneş, H., Shirsath, S.E., Baykal, A., 2015. Electrical properties and hyperfine interactions of boron doped Fe3O4 nanoparticles. Superlattices Microstruct. 88, 450–466. https://doi.org/10.1016/j.spmi.2015.10.005

Baykal, A., Amir, Md., Günerb, S., Sözeri, H., 2015. Preparation and characterization of SPION functionalized via caffeic acid. J. Magn. Magn. Mater. 395, 199–204. https://doi.org/10.1016/j.jmmm.2015.07.095

Bée, A., Obeid, L., Mbolantenaina, R., Welschbillig, M., Talbot, D., 2017. Magnetic chitosan/clay beads: A magsorbent for the removal of cationic dye from water. J. Magn. Magn. Mater. 421, 59–64. https://doi.org/10.1016/j.jmmm.2016.07.022

Boucherit, N., Delichere, P., Joiret, S., Hugot le Goff, A., 1989. Passivity of Iron and Iron Alloys Studied by Voltammetry and Raman Spectroscopy. Mater. Sci. Forum 44–45, 51–62. https://doi.org/10.4028/www.scientific.net/MSF.44-45.51

Byrne, J.M., Coker, V.S., Moise, S., Wincott, P.L., Vaughan, D.J., Tuna, F., Arenholz, E., van der Laan, G., Pattrick, R.A.D., Lloyd, J.R., Telling, N.D., 2013. Controlled cobalt doping in biogenic magnetite nanoparticles. J. R. Soc. Interface 10, 20130134. https://doi.org/10.1098/rsif.2013.0134

Chang, P.R., Yu, J., Ma, X., Anderson, D.P., 2011. Polysaccharides as stabilizers for the synthesis of magnetic nanoparticles. Carbohydr. Polym. 83, 640–644. https://doi.org/10.1016/j.carbpol.2010.08.027

Cornell, R.M., Schwertmann, U., 2003. The iron oxides: structure, properties, reactions, occurrences, and uses, 2nd, completely rev. and extended ed ed. Wiley-VCH, Weinheim.

Covaliu, C.I., Berger, D., Matei, C., Diamandescu, L., Vasile, E., Cristea, C., Ionita, V., Iovu, H., 2011. Magnetic nanoparticles coated with polysaccharide polymers for potential biomedical applications. J. Nanoparticle Res. 13, 6169–6180. https://doi.org/10.1007/s11051-011-0452-6

Culita, D.C., Marinescu, G., Patron, L., Carp, O., Cizmas, C.B., Diamandescu, L., 2008. Superparamagnetic nanomagnetites modified with histidine and tyrosine. Mater. Chem. Phys. 111, 381–385. https://doi.org/10.1016/j.matchemphys.2008.04.033

Dai, Q., Nelson, A., 2010. Magnetically-responsive self assembled composites. Chem. Soc. Rev. 39, 4057. https://doi.org/10.1039/b812669k

Daniels, J.M., Rosencwaig, A., 1969. Mössbauer spectroscopy of stoichiometric and non-stoichiometric magnetite. J. Phys. Chem. Solids 30, 1561–1571. https://doi.org/10.1016/0022-3697(69)90217-0

Daou, T.J., Begin-Colin, S., Grenèche, J.M., Thomas, F., Derory, A., Bernhardt, P., Legaré, P., Pourroy, G., 2007. Phosphate Adsorption Properties of Magnetite-Based Nanoparticles. Chem. Mater. 19, 4494–4505. https://doi.org/10.1021/cm071046v

Daou, T.J., Grenèche, J.M., Pourroy, G., Buathong, S., Derory, A., Ulhaq-Bouillet, C., Donnio, B., Guillon, D., Begin-Colin, S., 2008. Coupling Agent Effect on Magnetic Properties of Functionalized Magnetite-Based Nanoparticles. Chem. Mater. 20, 5869–5875. https://doi.org/10.1021/cm801405n

Daou, T.J., Pourroy, G., Bégin-Colin, S., Grenèche, J.M., Ulhaq-Bouillet, C., Legaré, P., Bernhardt, P., Leuvrey, C., Rogez, G., 2006. Hydrothermal Synthesis of Monodisperse Magnetite Nanoparticles. Chem. Mater. 18, 4399–4404. https://doi.org/10.1021/cm060805r

de Faria, D.L.A., Venâncio Silva, S., de Oliveira, M.T., 1997. Raman microspectroscopy of some iron oxides and oxyhydroxides. J. Raman Spectrosc. 28, 873–878. https://doi.org/10.1002/(SICI)1097-4555(199711)28:11<873::AID-JRS177>3.0.CO;2-B

Dormann, J.L., Fiorani, D., Tronc, E., 1999. On the models for interparticle interactions in nanoparticle assemblies: comparison with experimental results. J. Magn. Magn. Mater. 202, 251–267. https://doi.org/10.1016/S0304-8853(98)00627-1

Eivazzadeh-Keihan, R., Bahreinizad, H., Amiri, Z., Aliabadi, H.A.M., Salimi-Bani, M., Nakisa, A., Davoodi, F., Tahmasebi, B., Ahmadpour, F., Radinekiyan, F., Maleki, A., Hamblin, M.R., Mahdavi, M., Madanchi, H., 2021. Functionalized magnetic nanoparticles for the separation

and purification of proteins and peptides. TrAC Trends Anal. Chem. 141, 116291. https://doi.org/10.1016/j.trac.2021.116291
Filippov, L.O., Severov, V.V., Filippova, I.V., 2013. Mechanism of starch adsorption on Fe–Mg–Al-bearing amphiboles. Int. J. Miner. Process. 123, 120–128. https://doi.org/10.1016/j.minpro.2013.05.010
Fock, J., Hansen, M.F., Frandsen, C., Mørup, S., 2018. On the interpretation of Mössbauer spectra of magnetic nanoparticles. J. Magn. Magn. Mater. 445, 11–21. https://doi.org/10.1016/j.jmmm.2017.08.070
Gnanaprakash, G., Mahadevan, S., Jayakumar, T., Kalyanasundaram, P., Philip, J., Raj, B., 2007a. Effect of initial pH and temperature of iron salt solutions on formation of magnetite nanoparticles. Mater. Chem. Phys. 103, 168–175. https://doi.org/10.1016/j.matchemphys.2007.02.011
Gnanaprakash, G., Philip, J., Jayakumar, T., Raj, B., 2007b. Effect of Digestion Time and Alkali Addition Rate on Physical Properties of Magnetite Nanoparticles. J. Phys. Chem. B 111, 7978–7986. https://doi.org/10.1021/jp071299b
Güner, S., Baykal, A., Amir, Md., Güngüneş, H., Geleri, M., Sözeri, H., Shirsath, S.E., Sertkol, M., 2016. Synthesis and characterization of oleylamine capped MnxFe1-xFe2O4 nanocomposite: Magneto-optical properties, cation distribution and hyperfine interactions. J. Alloys Compd. 688, 675–686. https://doi.org/10.1016/j.jallcom.2016.07.033
Hah, H.Y., Gray, S., Johnson, C.E., Johnson, J.A., Kolesnichenko, V., Kucheryavy, P., Goloverda, G., 2021. Mössbauer spectroscopy of superparamagnetic Fe3O4 nanoparticles. J. Magn. Magn. Mater. 539, 168382. https://doi.org/10.1016/j.jmmm.2021.168382
Han, D.H., Wang, J.P., Luo, H.L., 1994. Crystallite size effect on saturation magnetization of fine ferrimagnetic particles. J. Magn. Magn. Mater. 136, 176–182. https://doi.org/10.1016/0304-8853(94)90462-6
Hanesch, M., 2009. Raman spectroscopy of iron oxides and (oxy)hydroxides at low laser power and possible applications in environmental magnetic studies. Geophys. J. Int. 177, 941–948. https://doi.org/10.1111/j.1365-246X.2009.04122.x
Hernández, R., Sacristán, J., Nogales, A., Ezquerra, T.A., Mijangos, C., 2009. Structural Organization of Iron Oxide Nanoparticles Synthesized Inside Hybrid Polymer Gels Derived from Alginate Studied with Small-Angle X-ray Scattering. Langmuir 25, 13212–13218. https://doi.org/10.1021/la902441s
Hong, J., Xu, D., Yu, J., Gong, P., Ma, H., Yao, S., 2007. Facile synthesis of polymer-enveloped ultrasmall superparamagnetic iron oxide for magnetic resonance imaging. Nanotechnology 18, 135608. https://doi.org/10.1088/0957-4484/18/13/135608
Iyengar, S.J., Joy, M., Mohamed, A.P., Samanta, S., Ghosh, C.K., Ghosh, S., 2016. Fabrication of magnetite nanocrystals in alcohol/water mixed solvents: catalytic and colloid property evaluation. RSC Adv. 6, 60845–60855. https://doi.org/10.1039/C6RA11225K
Jacintho, G.V.M., Corio, P., Rubim, J.C., 2007. Surface-enhanced Raman spectra of magnetic nanoparticles adsorbed on a silver electrode. J. Electroanal. Chem. 603, 27–34. https://doi.org/10.1016/j.jelechem.2007.02.019
Jolivet, J.-P., Henry, M., Livage, J., 2000. Metal oxide chemistry and synthesis: from solution to solid state. John Wiley, Chichester ; New York.
Jones, F., Cölfen, H., Antonietti, M., 2000. Iron oxyhydroxide colloids stabilized with polysaccharides. Colloid Polym. Sci. 278, 491–501. https://doi.org/10.1007/s003960050546
K. Lagarec, Rancourt, D.G., 1998. Recoil - Mössbauer Spectral Analysis Software for Windows, version 1.02.
Kaihara, S., Suzuki, Y., Fujimoto, K., 2011. In situ synthesis of polysaccharide nanoparticles via polyion complex of carboxymethyl cellulose and chitosan. Colloids Surf. B Biointerfaces 85, 343–348. https://doi.org/10.1016/j.colsurfb.2011.03.008
Kotsikau, D., Pankov, V., Petrova, E., Natarov, V., Filimonov, D., Pokholok, K., 2018. Structural, magnetic and hyperfine characterization of Zn x Fe 3–x O 4 nanoparticles prepared by sol-gel

approach via inorganic precursors. J. Phys. Chem. Solids 114, 64–70. https://doi.org/10.1016/j.jpcs.2017.11.004
Kumar, C.S.S.R. (Ed.), 2012. Raman spectroscopy for nanomaterials characterization. Springer, Berlin.
LaMer, V.K., Dinegar, R.H., 1950. Theory, Production and Mechanism of Formation of Monodispersed Hydrosols. J. Am. Chem. Soc. 72, 4847–4854. https://doi.org/10.1021/ja01167a001
Laskowski, J.S., Liu, Q., O'Connor, C.T., 2007. Current understanding of the mechanism of polysaccharide adsorption at the mineral/aqueous solution interface. Int. J. Miner. Process. 84, 59–68. https://doi.org/10.1016/j.minpro.2007.03.006
Li, L., Zhang, C., Yuan, Z., Xu, X., Song, Z., 2019. AFM and DFT study of depression of hematite in oleate-starch-hematite flotation system. Appl. Surf. Sci. 480, 749–758. https://doi.org/10.1016/j.apsusc.2019.02.224
Liang, Q., Zhao, D., Qian, T., Freeland, K., Feng, Y., 2012. Effects of Stabilizers and Water Chemistry on Arsenate Sorption by Polysaccharide-Stabilized Magnetite Nanoparticles. Ind. Eng. Chem. Res. 51, 2407–2418. https://doi.org/10.1021/ie201801d
Ma, X., 2008. Role of solvation energy in starch adsorption on oxide surfaces. Colloids Surf. Physicochem. Eng. Asp. 320, 36–42. https://doi.org/10.1016/j.colsurfa.2008.01.011
Maccarini, M., Atrei, A., Innocenti, C., Barbucci, R., 2014. Interactions at the CMC/magnetite interface: Implications for the stability of aqueous dispersions and the magnetic properties of magnetite nanoparticles. Colloids Surf. Physicochem. Eng. Asp. 462, 107–114. https://doi.org/10.1016/j.colsurfa.2014.08.026
Meite, F., Abdelmoula, M., Billard, P., Hauet, T., Zegeye, A., 2022a. Pb-Bearing Ferrihydrite Bioreduction and Secondary-Mineral Precipitation during Fe Redox Cycling. Minerals 12, 610. https://doi.org/10.3390/min12050610
Meite, F., Hauet, T., Billard, P., Ferté, T., Abdelmoula, M., Zegeye, A., 2022b. Insight into the magnetic properties of Pb-dopped iron oxide nanoparticles during Fe(III) bio-reduction by Shewanella oneidensis MR-1. Chem. Geol. 606, 120904. https://doi.org/10.1016/j.chemgeo.2022.120904
Miyamoto, Y., Koshidaka, Y., Noguchi, H., Oishi, K., Saito, H., Yukawa, H., Kaji, N., Ikeya, T., Iwata, H., Baba, Y., Murase, K., Hayashi, S., 2012. Polysaccharide Functionalized Magnetic Nanoparticles for Cell Labeling and Tracking: A New Three-Dimensional Cell-Array System for Toxicity Testing, in: Nagarajan, R. (Ed.), ACS Symposium Series. American Chemical Society, Washington, DC, pp. 191–208. https://doi.org/10.1021/bk-2012-1119.ch009
Mørup, S., Bo Madsen, M., Franck, J., Villadsen, J., Koch, C.J.W., 1983. A new interpretation of Mössbauer spectra of microcrystalline goethite: "Super-ferromagnetism" or "super-spin-glass" behaviour? J. Magn. Magn. Mater. 40, 163–174. https://doi.org/10.1016/0304-8853(83)90024-0
Mørup, S., Hansen, M.F., Frandsen, C., 2010. Magnetic interactions between nanoparticles. Beilstein J. Nanotechnol. 1, 182–190. https://doi.org/10.3762/bjnano.1.22
Mutaftschiev, B., 2001. The Atomistic Nature of Crystal Growth.
Néel, L., 1949. Théorie du traînage magnétique des ferromagnétiques en grains fins avec application aux terres cuites. Ann. Géophysique 5, 99–136.
Ohtsuka, T., Kubo, K., Sato, N., 1986. Raman Spectroscopy of Thin Corrosion Films on Iron at 100 to 150 C in Air. CORROSION 42, 476–481. https://doi.org/10.5006/1.3583054
Pattanaik, A., Venugopal, R., 2018. Investigation of Adsorption Mechanism of Reagents (Surfactants) System and its Applicability in Iron Ore Flotation – An Overview. Colloid Interface Sci. Commun. 25, 41–65. https://doi.org/10.1016/j.colcom.2018.06.003
Rakotomalala Robinson, M., Abdelmoula, M., Mallet, M., Coustel, R., 2019. Starch functionalized magnetite nanoparticles: New insight into the structural and magnetic properties. J. Solid State Chem. 277, 587–593. https://doi.org/10.1016/j.jssc.2019.06.033
Rakotomalala Robinson, M., Coustel, R., Abdelmoula, M., Mallet, M., 2020. As(V) and As(III) sequestration by starch functionalized magnetite nanoparticles: influence of the synthesis route onto the trapping efficiency. Sci. Technol. Adv. Mater. 21, 524–539. https://doi.org/10.1080/14686996.2020.1782714

Rashid, Md.H., Raula, M., Mandal, T.K., 2014. Synthesis of magnetic nanostructures: Shape tuning by the addition of a polymer at low temperature. Mater. Chem. Phys. 145, 491–498. https://doi.org/10.1016/j.matchemphys.2014.03.002

Ren, G., Wang, X., Huang, P., Zhong, B., Zhang, Z., Yang, L., Yang, X., 2017. Chromium (VI) adsorption from wastewater using porous magnetite nanoparticles prepared from titanium residue by a novel solid-phase reduction method. Sci. Total Environ. 607–608, 900–910. https://doi.org/10.1016/j.scitotenv.2017.06.103

Sarkar, D., Mandal, M., 2012. Static and Dynamic Magnetic Characterization of DNA-Templated Chain-Like Magnetite Nanoparticles. J. Phys. Chem. C 116, 3227–3234. https://doi.org/10.1021/jp208020z

Sawatzky, G.A., Coey, J.M.D., Morrish, A.H., 1969. Mössbauer Study of Electron Hopping in the Octahedral Sites of Fe_3O_4. J. Appl. Phys. 40, 1402–1403. https://doi.org/10.1063/1.1657689

Scherrer, P., n.d. Bestimmung der Grosse und der Inneren Struktur von Kolloidteilchen Mittels Rontgenstrahlen. Nachrichten Von Ges. Wiss. Zu Gött. Math.-Phys. Kl. 1918, 98–100.

Schwertmann, U., Cornell, R.M. (Eds.), 2000. Iron Oxides in the Laboratary. Wiley-VCH Verlag GmbH, Weinheim, Germany. https://doi.org/10.1002/9783527613229

Shebanova, O.N., Lazor, P., 2003. Raman spectroscopic study of magnetite (FeFe2O4): a new assignment for the vibrational spectrum. J. Solid State Chem. 174, 424–430. https://doi.org/10.1016/S0022-4596(03)00294-9

Srivastava, C.M., Shringi, S.N., Babu, M.V., 1981. Mössbauer study of the low-temperature phase of magnetite. Phys. Status Solidi A 65, 731–735. https://doi.org/10.1002/pssa.2210650241

Suryanarayana, C., Norton, M.G., 2014. X-Ray Diffraction: A Practical Approach. Springer Verlag.

Tronc, E., Prene, P., Jolivet, J.P., d'Orazio, F., Lucari, F., Fiorani, D., Godinho, M., Cherkaoui, R., Nogues, M., Dormann, J.L., 1995. Magnetic behaviour of γ-Fe2O3 nanoparticles by mössbauer spectroscopy and magnetic measurements. Hyperfine Interact. 95, 129–148. https://doi.org/10.1007/BF02146310

Uthaman, S., Lee, S.J., Cherukula, K., Cho, C.-S., Park, I.-K., 2015. Polysaccharide-Coated Magnetic Nanoparticles for Imaging and Gene Therapy. BioMed Res. Int. 2015, 1–14. https://doi.org/10.1155/2015/959175

Vandenberghe, R.E., Barrero, C.A., da Costa, G.M., Van San, E., De Grave, E., 2000. Mössbauer characterization of iron oxides and (oxy)hydroxides: the present state of the art. Hyperfine Interact. 126, 247–259. https://doi.org/10.1023/A:1012603603203

Verwey, E.J.W., 1939. Electronic Conduction of Magnetite (Fe3O4) and its Transition Point at Low Temperatures. Nature 144, 327–328. https://doi.org/10.1038/144327b0

Wang, Y., Li, B., Zhou, Y., Jia, D., 2008. Chitosan-induced synthesis of magnetite nanoparticles via iron ions assembly. Polym. Adv. Technol. 19, 1256–1261. https://doi.org/10.1002/pat.1121

Weissenborn, P.K., Warren, L.J., Dunn, J.G., 1995. Selective flocculation of ultrafine iron ore 2. Mechanism of selective flocculation. Colloids Surf. Physicochem. Eng. Asp. 99, 29–43. https://doi.org/10.1016/0927-7757(95)03112-Q

Yoon, Y., Zheng, M., Ahn, Y.-T., Park, W.K., Yang, W.S., Kang, J.-W., 2017. Synthesis of magnetite/non-oxidative graphene composites and their application for arsenic removal. Sep. Purif. Technol. 178, 40–48. https://doi.org/10.1016/j.seppur.2017.01.025

Zegeye, A., Abdelmoula, M., Usman, M., Hanna, K., Ruby, C., 2011. In situ monitoring of lepidocrocite bioreduction and magnetite formation by reflection Mossbauer spectroscopy. Am. Mineral. 96, 1410–1413. https://doi.org/10.2138/am.2011.3794

Zegeye, A., Carteret, C., Mallet, M., Billet, D., Ferté, T., Chang, C.S., Hauet, T., Abdelmoula, M., 2021. Effect of Sb on precipitation of biogenic minerals during the reduction of Sb-bearing ferrihydrites. Geochim. Cosmochim. Acta 309, 96–111. https://doi.org/10.1016/j.gca.2021.06.021

Zhang, J., Shin, M.C., David, A.E., Zhou, J., Lee, K., He, H., Yang, V.C., 2013. Long-Circulating Heparin-Functionalized Magnetic Nanoparticles for Potential Application as a Protein Drug Delivery Platform. Mol. Pharm. 10, 3892–3902. https://doi.org/10.1021/mp400360q

Zhang, Q., Yang, X., Guan, J., 2019. Applications of Magnetic Nanomaterials in Heterogeneous Catalysis. ACS Appl. Nano Mater. 2, 4681–4697. https://doi.org/10.1021/acsanm.9b00976
Zhu, Y., Chen, K., Wang, X., Guo, X., 2012. Spherical polyelectrolyte brushes as a nanoreactor for synthesis of ultrafine magnetic nanoparticles. Nanotechnology 23, 265601. https://doi.org/10.1088/0957-4484/23/26/265601

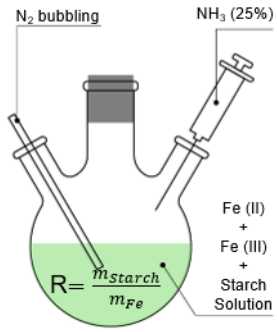

Fig. 1. Schematic presentation of synthesis of starch functionalized nano magnetites by coprecipitation method.

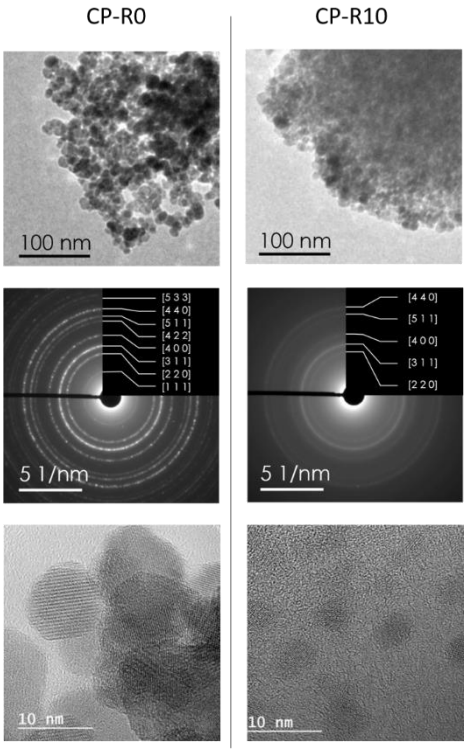

Fig. 2. TEM micrographs and SEAD patterns of CP-R0 and CP-R10.

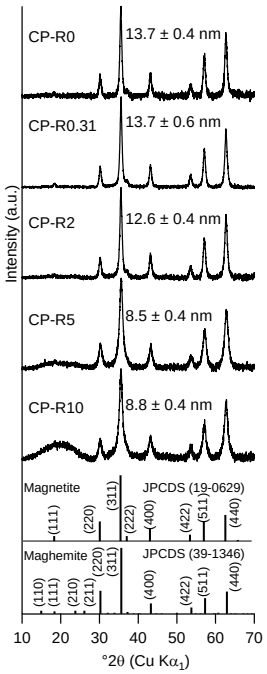

Fig. 3. PXRD patterns of the as-synthetized CP products at different R values and corresponding crystallite size determined from Scherrer's formula.

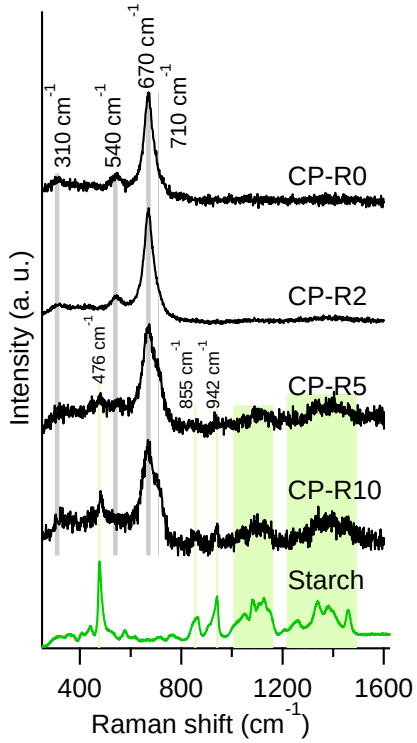

Fig. 4. Raman spectra of CP products and native starch.

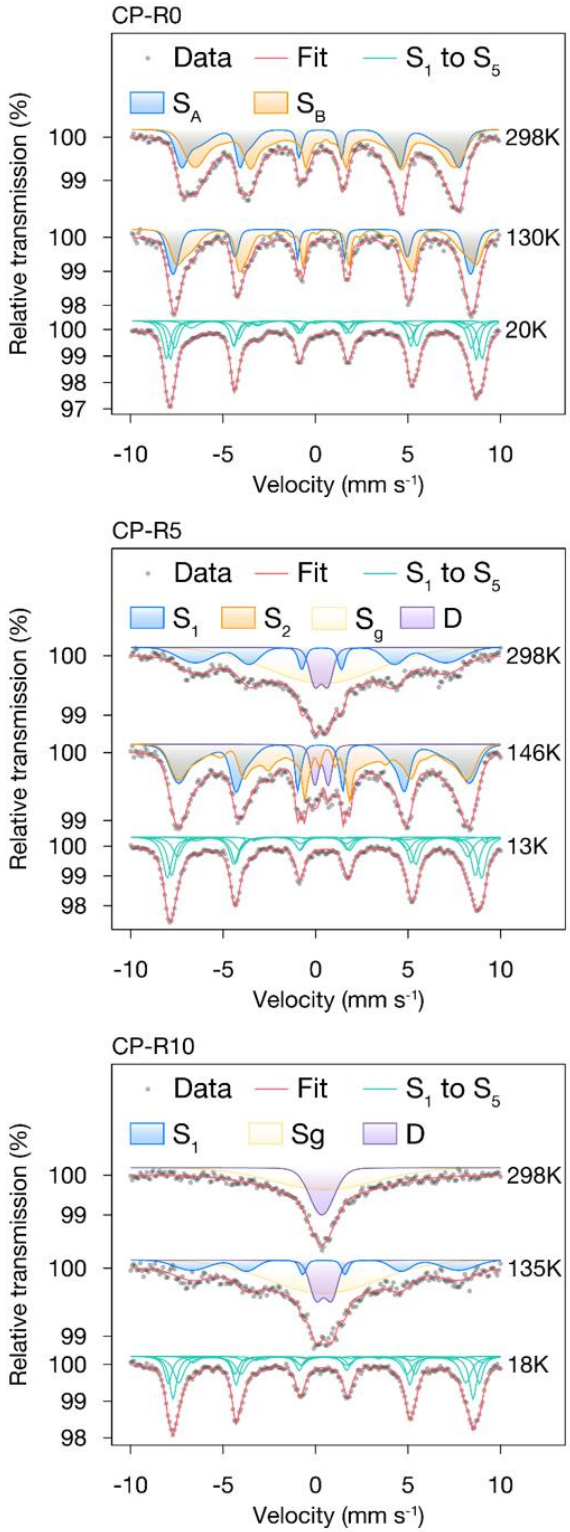

Fig. 5. Mössbauer spectra of CP-R0, CP-R5, CP-R10 between room temperature and 13 K.

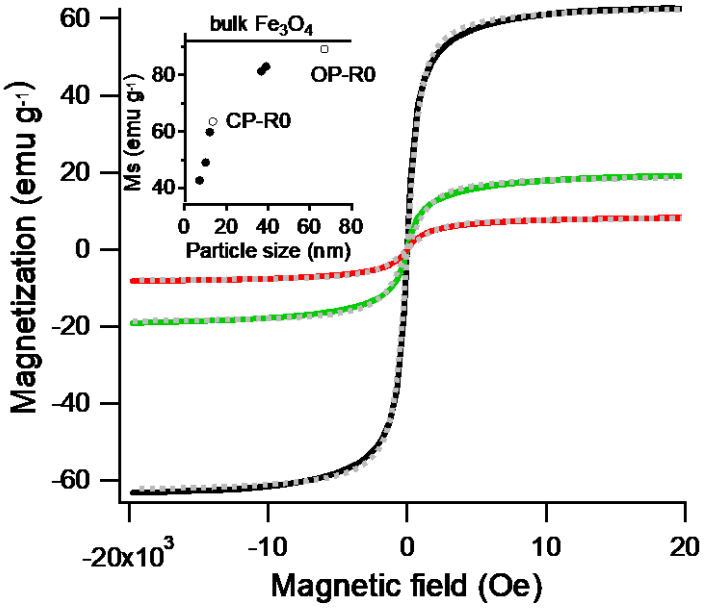

Fig. 6: Magnetic hysteresis loops at room temperature of CP-R0 (black), CP-R5 (green) and CP-R10 (red) and Langevin function fits (dashed line). Inset: magnetization at saturation for Fe_3O_4 NP (open symbol this work, filled symbol see ref in text).

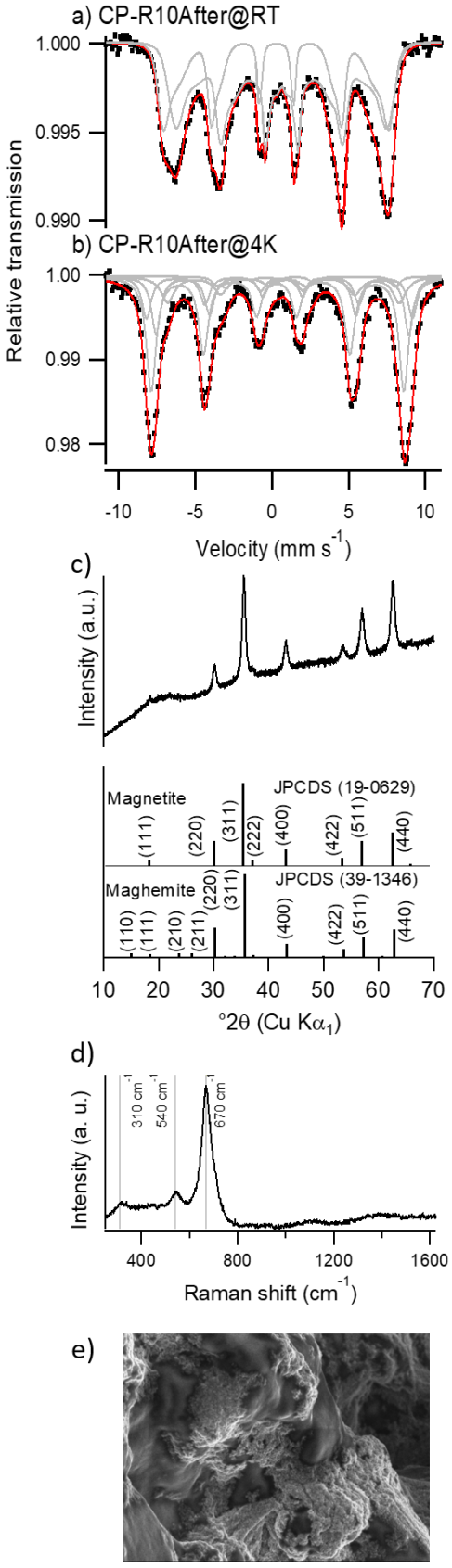

Fig. 7. Mössbauer spectra recorded at room temperature (a) and 4 K (b), PXRD pattern (c), Raman spectrum (d) and SEM image (e) of CP-R10After.

Table 1. Mössbauer hyperfine parameters for the as-synthetized products (values obtained after fitting the experimental data).

Sample	Site	CS (mm s^{-1})	ε or Δ (mm s^{-1})	H_{hf} or $<H_{hf}>$ (T)	RA (%)
CP-R0@RT	S_A	0.27	0.01	44.0	38
	S_B	0.54	-0.03	35.1	62
CP-R0@130K	S_A	0.33	0.02	49.9	35
	S_B	0.59	0.01	45.9	65
CP-R0@20K	S_1	0.41	0.1	51.9	14
	S_2	0.45	-0.01	50.5	45
	S_3	0.53	-0.03	53.2	25
	S_4	0.73	-0.07	46.3	12
	S_5	0.90	1.72	34.9	4
CP-R5@RT	S_1	0.30	-0.03	42.0	32
	D	0.31	0.69	-	13
	S_g	0.38	-	-	56
CP-R5@146K	S_1	0.35	0.10	46.4	41
	S_2	0.51	-0.12	37.0	52
	D	0.32	0.73	-	7
CP-R5@13K	S_1	0.43	0.01	50.9	30
	S_2	0.43	-0.02	48.7	21
	S_3	0.50	-0.00	52.7	42
	S_4	0.65	0.08	44.2	5
	S_5	0.90	1.25	34.0	2
CP-R10@RT	D	0.34	0.98	-	34
	Sg	0.50	-	-	66
CP-R10@135	S_1	0.49	0.03	44.7	24
	D	0.44	0.87	-	17
	S_g	0.43	-	-	59
CP-R10@18K	S_1	0.41	0	50.3	35
	S_2	0.42	0	48.1	33
	S_3	0.48	-0.04	52.1	22
	S_4	0.92	0.27	48.4	7
	S_5	1.21	0.87	33.1	3
CP-R10After@RT	S_A	0.28	0	43.0	36
	S_B	0.62	-0.01	32.2	64
CP-R10After@4K	S_1	0.33	0.03	51.1	45
	S_2	0.57	-0.08	53.8	16
	S_3	0.69	-0.01	51.1	21
	S_4	0.89	-0.14	46.9	14
	S_5	1.05	1.50	34.2	4
OP-R0@RT	S_A	0.29	0.00	49.0	35
	S_B	0.66	0.00	45.8	65
OP-R0@4K	S_1	0.44	0.03	50.4	46
	S_2	0.47	0.03	54.1	12
	S_3	0.71	-0.23	52.5	13
	S_4	0.82	-0.22	47.4	19
	S_5	1.03	1.37	34.1	10